Nanoscale

PAPER

View Article Online
View Journal | View Issue

Cite this: *Nanoscale*, 2019, **11**, 2374

Titania-coated 2D gold nanoplates as nanoagents for synergistic photothermal/sonodynamic therapy in the second near-infrared window†

Fengli Gao, Guangli He, Hang Yin, Jian Chen, Yibiao Liu, Chong Lan, Shouren Zhang * and Baocheng Yang

The development of efficient nanomedicines to improve anticancer therapeutic effects is highly attractive. In this work, we firstly report titania-coated Au nanoplate (Au NPL@TiO_2) heterostructures, which play dual roles as nanoagents for synergistic photothermal/sonodynamic therapy in the second near-infrared (NIR) window. On the one hand, because the controlled TiO_2 shells endow the Au NPL@TiO_2 nanostructures with a red shift to the NIR II region, the as-prepared Au NPL@TiO_2 nanostructures possess a high photothermal conversion efficiency of 42.05% when irradiated by a 1064 nm laser and are anticipated to be very promising candidates as photothermal agents. On the other hand, the Au nanoplates (Au NPLs), as electron traps, vastly improve the generation of reactive oxygen species (ROS) by the Au NPL@TiO_2 nanostructures in contrast with pure TiO_2 shell nanoparticles upon activation by ultrasound (US) *via* a sonodynamic process. Moreover, the toxicity and therapeutic effect of the Au NPL@TiO_2 nanostructures were relatively systemically evaluated *in vitro*. The Au NPL@TiO_2 nanostructures generate a large amount of intracellular ROS and exhibit laser power density-dependent toxicity, which eventually induces apoptosis of cancer cells. Furthermore, a synergistic therapeutic effect, with a cell viability of only 20.3% upon both photothermal and sonodynamic activation, was achieved at low concentrations of the Au NPL@TiO_2 nanostructures. Experiments on mice also demonstrate the superiority of the combination of PTT and SDT, with the total elimination of tumors. This work provides a way of applying two-dimensional (2D) gold nanoplate core/TiO_2 shell nanostructures as novel nanoagents for advanced multifunctional anticancer therapies in the second NIR window.

Received 4th September 2018,
Accepted 5th January 2019

DOI: 10.1039/c8nr07188h

rsc.li/nanoscale

Introduction

Cancer is a severe disease that jeopardizes the health and life of human beings. Photothermal therapy (PTT), which comprises strong local heating under laser irradiation for the elimination of tumours, has great potential for applications in cancer therapy. Near-infrared (NIR) light, as an external trigger, is more able to efficiently penetrate biological tissues than visible light and has been intensively employed in PTT owing to its high specificity for tumour sites, deeper tissue penetration and considerable therapeutic effects.[1,2] In the NIR region, two optical windows in biological tissues are located in the NIR I (650 nm–950 nm) and NIR II (1000 nm–1350 nm) regions, respectively.[3] Although traditional NIR I light has a greatly increased penetration depth in comparison with visible-range light owing to reduced tissue absorption and scattering, it is still not satisfactory for applications in clinical medicine.[4,5] The growing interest in photoinduced therapy of tumours has moved toward the longer-wavelength NIR II window, which allows a longer maximum permissible exposure (MPE) and a desirable tissue penetration depth.[6–8] Currently, a great number of photoactivated nanomaterials are widely studied as tumour-imaging agents for use in the NIR II region,[4,9–11] but there is still a dearth of NIR II-induced PTT agents with strong absorption and effective photothermal conversion for the successful treatment of tumours.

Sonodynamic therapy (SDT), as another emerging platform that represents a non-invasive manner of eradicating solid tumours, has also received enormous attention in clinical therapy.[12,13] When triggered by external ultrasound (US) energy, a sonosensitizer can be activated to generate toxic ROS, including hydroxyl radicals ($^{\bullet}OH$) and singlet oxygen ($^1O_2$), for the further apoptosis and obliteration of cancer cells.[14–16] In contrast to visible light in photodynamic therapy, US, as a

Henan Provincial Key Laboratory of Nanocomposites and Applications, Institute of Nanostructured Functional Materials, Huanghe Science and Technology College, Zhengzhou, Henan 450006, China. E-mail: shourenzhang@infm.hhstu.edu.cn

†Electronic supplementary information (ESI) available: Size distribution of Au cores/TiO_2 shells with different shell thicknesses, SEM of Au NPL@TiO_2 nanostructures, UV-vis spectrum of TiO_2 shell nanoparticles, the reaction between DPBF and $^1O_2$ and the reaction of TA and $^{\bullet}OH$. See DOI: 10.1039/c8nr07188h

mechanical wave, is regarded as much safer and enables better tissue penetration with limited energy attenuation. Furthermore, US can precisely target and achieve the activation of a sonosensitizer at a tumour site, which facilitates the destruction of solid tumours.[17] Pure TiO_2 nanoparticles have been demonstrated to be stable sonosensitizers with high biocompatibility and have been widely used in sonodynamic therapy.[18] Nevertheless, owing to the low yield of ROS, which results from fast electron–hole recombination, much effort has been directed toward the study of noble metal-modified TiO_2 nanostructures, such as Ag-TiO_2 [19] and Au-TiO_2,[20] in the field of photocatalysis and light harvesting. Unfortunately, in the field of sonodynamic therapy, previous research on metal-modified TiO_2 nanostructures mainly focused on single treatment and the ultrasound power used was much higher,[12] even reaching 30 W, and metal-TiO_2 nanostructures for combined synergistic cancer therapy with an excellent therapeutic effect at a safe power are still rarely investigated.

Gold nanocrystals have been studied continuously for many years and have attracted much attention thanks to their unique strong local surface plasmon resonance (LSPR) in the visible-light region, which has enabled their widespread use in biosensors,[21] photocatalysis,[22] cancer therapeutics[23] and tumor imaging.[24] In particular, in cancer therapy gold nanocrystals, including Au nanorods,[25] Au nanospheres,[26] Au nanorings,[27] Au nanoechinuses[2] and Au nanocages,[28] exhibited excellent PTT effects in the NIR I window. However, NIR II absorbers are rarely mentioned for PTT based on gold nanocrystals, despite various surface modifications. Au nanoplates are the ideal metal nanostructures for tunable optical properties associated with their geometrical structure.[29,30] Their abundant plasmon resonance modes and the strong electric field at the sharp corners of Au NPLs also enable further applications in sensing and optoacoustic imaging.[31–36] Nevertheless, little attention is paid to the utilization of Au NPLs as photothermal agents, in particular in the second biological window.

In this study, we successfully synthesized an antitumour therapeutic agent based on Au NPL@TiO_2 nanostructures with controllable shell thicknesses (Scheme 1). By modifying the TiO_2 shells in the surfaces of 2D Au NPLs, the Au NPL@TiO_2 nanostructures exhibited a red shift from the NIR I to the NIR II region, displayed strong absorbance at 1064 nm, and exhibited a photothermal conversion efficiency of 42.05%. Moreover, under exposure to US, the Au NPL@TiO_2 nanostructures provided a charge transfer channel at the metal–semiconductor interface, and the Au NPLs could extensively suppress the recombination of pairs of electrons (e^-) and holes (h^+) generated from TiO_2, which led to an enhancement in the generation of ROS in comparison with pure TiO_2 nanoparticles. We demonstrated that the Au NPL@TiO_2 nanostructures exhibited extraordinary biocompatibility and ability to generate intracellular ROS. Moreover, *in vitro* and *in vivo* studies suggested that the Au NPL@TiO_2 nanostructures can be employed as anticancer agents in a combination of PTT with SDT for the highly efficient treatment of cancer.

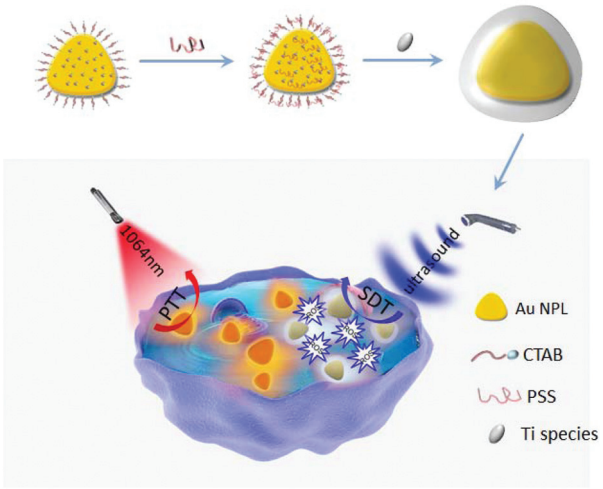

Scheme 1 Illustration of synthesis of Au NPL@TiO_2 nanostructures and synergetic photothermal/sonodynamic therapy against HeLa cells.

Experimental

Synthesis of Au NPLs

Au NPLs were prepared by a seed-mediated growth method, as previously reported. The seed solution was prepared by adding 1 mL $HAuCl_4$ (0.1 M) and 1 mL trisodium citrate (0.01 M) to 36 mL water, and then 1 mL fresh $NaBH_4$ (0.1 M) was added to the mixture under vigorous stirring. The resulting solution was kept for 3 h at room temperature. In the meantime, the growth solutions were prepared. Growth solution 1 and growth solution 2 were identical and were obtained by mixing 9 mL cetyltrimethylammonium bromide (CTAB, 0.05 M), 250 μL $HAuCl_4$ (0.01 M), 50 μL NaOH (0.1 M), 50 μL KI (0.01 M) and 50 μL ascorbic acid (AA, 0.1 M). Growth solution 3 was prepared by mixing 90 mL CTAB (0.05 M), 2.5 mL $HAuCl_4$ (0.01 M), 0.5 mL NaOH (0.1 M), 0.5 mL KI (0.05 M) and 0.5 mL AA (0.1 M). To synthesize Au NPLs, 0.6 mL seed solution was quickly added to growth solution 1 and gently shaken for 5 s, and then 1 mL of the mixture with solution 1 was quickly added to solution 2. After gentle shaking for 5 s, the whole mixture with solution 2 was added to solution 3 and then gently stirred for 10 s. The resulting solution was left undisturbed at room temperature overnight. On the following day, Au NPLs were precipitated to the bottom, and the supernatants were gently poured out thoroughly. Then, 20 mL water was added to disperse the Au NPLs in the flask.

Synthesis of Au NPL@TiO_2 nanostructures with different shell thicknesses and TiO_2 shell nanoparticles

The as-prepared Au NPLs solution (20 mL) after dispersion in water was added dropwise to 20 mL aqueous poly(sodium 4-styrenesulfonate) (PSS) solution (2 g L^{-1}, containing 6 mM NaCl) under vigorous stirring. The solution was stirred for 8 h and centrifuged at 7000 rpm for 15 min to remove excess PSS. Finally, the Au NPLs-PSS precipitates were dispersed in 200 μL water for use. To obtain Au NPL@TiO_2 nanostructures, 3 mL

water and 0.1 mL $TiCl_3$ were mixed in a vial, after which 0.43 mL $NaHCO_3$ (0.79 M) was dropped under rapid stirring. Then, 100 μL Au NPLs-PSS was added and stirred for 30 min at room temperature. The resulting solution of Au NPL@TiO_2 nanostructures was centrifuged and redispersed in 3.6 mL water. To control the thicknesses of different TiO_2 shells, the volume of $NaHCO_3$ was 0.43 mL, 0.45 mL, 0.48 mL and 0.50 mL, respectively. Thermal treatment of the washed core–shell nanostructures was carried out in a box furnace in air at 450 °C for 2 h with a ramp rate of 5 °C min^{-1}. The thermal treatment caused the amorphous shell to crystallize into anatase TiO_2.

To obtain TiO_2 shell nanoparticles, Au NPL@TiO_2 nanostructures underwent oxidative etching of the Au NPL core using an iodide-based liquid electrolyte, which contained 0.1 M LiI, 50 mM I_2, and 0.6 M 1,2-dimethyl-3-propylimidazolium iodide in acetonitrile/valeronitrile [85/15, v : v]. Firstly, 100 μL etching solution was added to 1 mL of a solution of Au NPL@TiO_2 nanostructures under shaking for 24 h. After that, the TiO_2 shell nanoparticles were centrifuged and dispersed in 1 mL water.

Photothermal conversion

The as-prepared solutions of Au NPL@TiO_2 nanostructures with various shell thicknesses (2 mL), namely, Au NPL@TiO_2-1, Au NPL@TiO_2-2, Au NPL@TiO_2-3 and Au NPL@TiO_2-4 nanostructures, were irradiated by a 1064 nm laser (1 W cm^{-2}, 5 min), respectively. A TES 1310 thermometer was used to monitor the changes in temperature, which was recorded at intervals of ten seconds. To calculate the photothermal conversion efficiency of the Au NPL@TiO_2-4 nanostructures, 2 mL Au NPL@TiO_2-4 nanostructures were irradiated by a 1064 nm laser for 5 min, and then the laser was turned off. The temperature changes were recorded during the laser-on and laser-off stages. The calculation of the photothermal conversion efficiency η_T was based on Roper's method:[7]

$$\eta_T = \frac{hA(T_{max} - T_{amb}) - Q_0}{I(1 - 10^{-A_\lambda})} \quad (1)$$

where Q_0 was measured independently to be 5.4×10^{-4} I; $(T_{max} - T_{amb})$ is 41.6 °C for Au NPL@TiO_2-4 nanostructures, according to Fig. 3a; I is the laser power of 785 mW; and A_λ is the absorbance of Au NPL@TiO_2-4 nanostructures (2.07) at 1064 nm. The value of hA was determined by the following formulae:

$$\theta = \frac{T - T_{amb}}{T_{max} - T_{amb}} \quad (2)$$

$$\tau_s = \frac{\sum_i m_i c_{pi}}{hA} \quad (3)$$

$$t = -\tau_s \ln(\theta) \quad (4)$$

Thus, the time constant for heat transfer from the system was determined to be τ_s = 160 s for the Au NPL@TiO_2 nanostructures, when the linear time data for the cooling period *versus* the negative natural logarithm of the temperature driving force were used (Fig. 3c). Here, m_i and c_{pi} are the mass (0.3 g) and heat capacity (4.2 J g^{-1}) of deionized water, respectively, and hA was calculated to be 7.87 mW $°C^{-1}$. Therefore, the photothermal conversion efficiency of Au NPL@TiO_2-4 nanostructures was 42.05%.

Detection of singlet oxygen ($^1O_2$) and hydroxyl radicals ($^{\cdot}OH$)

Au NPL@TiO_2 nanostructures after thermal treatment were dispersed in water by ultrasonication for 1 h to ensure good dispersion. 1,3-Diphenylisobenzofuran (DPBF) was used to monitor the generation of singlet oxygen induced by Au NPL@TiO_2 nanostructures, TiO_2 shell nanoparticles and Au NPLs.[7] Firstly, 1 mL of a solution of Au NPL@TiO_2 nanostructures (with different shell thicknesses), TiO_2 shell nanoparticles or Au NPLs was added to 2 mL DPBF (100 μM, dissolved in DMF) in a brown vial and exposed to US irradiation (1.5 W cm^{-2}, 3 MHz) for 20 min in the dark. After US irradiation, the solutions were centrifuged and the supernatants were analyzed by a UV-vis spectrometer. Hydroxyl radicals were detected by a terephthalic acid (TA) solution (500 μM in a 2 mM NaOH solution).[20] Firstly, 2 mL Au NPL@TiO_2 nanostructures, TiO_2 shell nanoparticles or Au NPLs was centrifuged and redispersed in the TA solution and then exposed to US irradiation (1.5 W cm^{-2}, 3 MHz) for 20 min in the dark. The fluorescence intensity was measured separately (excitation wavelength: 315 nm).

TGA (thermogravimetric analysis) measurements

Pure CTAB powder was analysed using an SDT Q600 TGA/DSC instrument for TGA analysis, and the temperature was increased from 20 °C to 500 °C at a rate of 5 °C min^{-1}.

Cytotoxicity test and ROS imaging *in vitro*

HeLa cells were cultured in a medium (MEM supplemented with 10% fetal bovine serum) at 37 °C in a humidified incubator under 5% CO_2. The cells were seeded into 96-well plates for 12 h to adhere at a density of 4×10^4 mL^{-1}. Various concentrations of calcined Au NPL@TiO_2 nanostructures with a shell thickness of 68 nm (0, 25, 50, 100, and 200 μg mL^{-1}) were co-incubated with HeLa cells for 24 h, and six replicates were used for each concentration. Then, 10 μL cell counting kit-8 (CCK-8) was added to each well to measure the cell viability at a wavelength of 450 nm after 90 min by a microplate reader. The cell viability (%) was calculated as $(A_{test}/A_{control}) \times 100$.

HeLa cells were seeded into 96-well plates and incubated with Au NPL@TiO_2 nanostructures for 24 h. Then, the HeLa cells were treated with US irradiation for 20 min (0.5 W cm^{-2}, 3 MHz, 4 min on/1 min off, repeated 5 times). Afterwards, the cell culture medium was replaced with 2,7-dichlorodihydrofluorescein diacetate (DCFH-DA, 10 μM, diluted with MEM), and the cells were incubated for a further 30 min in the dark. The cells were finally washed gently with PBS three times and observed by a fluorescence microscope in the dark.

Synergetic PTT and SDT for HeLa cells

HeLa cells were cultured in MEM supplemented with 10% fetal bovine serum at 37 °C in a humidified incubator under 5% CO_2 and were then seeded into 96-well plates for 12 h to adhere at a density of 4×10^4 mL^{-1}. Different groups of Au NPL@TiO_2 nanostructures, Au NPLs, and TiO_2 shell nanoparticles were co-cultured with HeLa cells for 24 h. Then, various treatments (laser, US, and laser + US) were performed on the experimental groups. In addition, to avoid the production of heat and ensure effective sonodynamic therapy, US treatment was administered intermittently as follows: 4 min on/1 min off, repeated 5 times. CCK-8 was employed to assess cell viability. The US power densities were 0.5, 1, and 1.5 W cm^{-2} and the laser power densities were 0.5, 1, and 1.5 W cm^{-2}, respectively.

HeLa cells were cultured in MEM supplemented with 10% fetal bovine serum at 37 °C in a humidified incubator under 5% CO_2 and were then seeded into 6-well plates for 12 h to adhere at a density of 2×10^6 mL^{-1}. Different groups of Au NPL@TiO_2 nanostructures, Au NPLs, and TiO_2 shell nanoparticles were co-cultured with HeLa cells for 24 h. Then, various treatments (laser, US, and laser + US) were performed on the experimental groups. Next, 10 μL calcein AM and 15 μL propidium iodide (PI) were added to 5 mL PBS to prepare a staining solution, and 1.5 mL staining solution was added to every well in a dark and incubated for 15 min. A confocal fluorescence microscope was used to observe live and dead cells.

Animal tumour models

Female nude mice (5 weeks old) bearing a HeLa tumour were subcutaneously injected with 1×10^7 cells under their left flank. *In vivo* studies were carried out 3 weeks after the inoculation with the tumor cells.

Synergistic therapy *in vivo*

The HeLa tumor-bearing mice were randomly divided into four groups (five mice per group) and then intravenously injected with the Au NPL@TiO_2 nanostructures (10 mg kg^{-1}), and mice in the control group were injected with PBS. After accumulation for 24 h, the mice in the experimental groups injected with Au NPL@TiO_2 nanostructures and mice in the control group were treated with ultrasound at a power density of 0.5 W cm^{-2} for 20 min (4 min on/1 min off, repeated 5 times) and irradiated with a 1064 nm laser at a power density of 1 W cm^{-2} for 5 min. The body weights of the mice were recorded at intervals of three days.

Results and discussion

Au NPLs were synthesized by a seed-mediated growth approach, as previously reported.[29] Fig. 1a and b show typical SEM and TEM images, respectively, of Au NPLs. The results showed the well-dispersed characteristics and uniform shapes of the Au NPLs in water, and their size was ~118 nm. Their height was confirmed from the AFM image in Fig. 1c, which

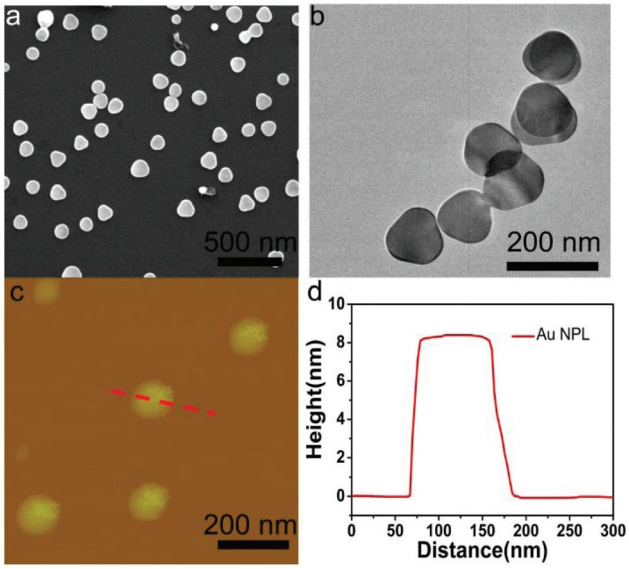

Fig. 1 Characterization of Au NPLs. (a) SEM, (b) TEM and (c) AFM images of Au NPLs. (d) Height profile determined along the red dashed line indicated in (c).

indicates a thickness of ~8.6 nm (Fig. 1d). The Au NPL@TiO_2 nanostructures are schematically illustrated in Scheme 1. The pre-grown Au NPLs capped with CTAB were firstly coated with an anionic PSS layer. $TiCl_3$ was then hydrolyzed to $Ti(OH)_3$ by $NaHCO_3$ and adsorbed on the PSS layer, followed by oxidation to TiO_2. Fig. 2a–j show TEM and SEM images and the extinction spectra and energy-dispersive X-ray spectrum (EDS) of four representative Au NPL@TiO_2 nanostructures with different shell thicknesses. Au NPL@TiO_2 nanostructures with increasing shell thicknesses were named as Au NPL@TiO_2-1, Au NPL@TiO_2-2, Au NPL@TiO_2-3 and Au NPL@TiO_2-4. At a fixed concentration of Ti^{3+}, the thickness of the TiO_2 shell could be varied in the range from 10 ± 2 nm to 68 ± 7 nm by changing the $NaHCO_3$ concentration (Fig. S1 and S2†). With an increase in the thickness of the TiO_2 shell, the plasmonic peak of the Au NPL@TiO_2 nanostructures was clearly red-shifted from 883 nm to 1055 nm in the case of Au NPL@TiO_2-4 nanoparticles.[20] The EDS also confirmed the formation of the Au NPL@TiO_2 nanostructures (Fig. 2j). Moreover, for comparison, TiO_2 shell nanoparticles were obtained from Au NPL@TiO_2-4 nanostructures by etching Au cores with hollow structures (Fig. 2k and S2†).

In order to determine the photothermal properties of Au NPL@TiO_2 nanostructures in the NIR II wavelength range, nanostructures with different shell thicknesses were irradiated with a 1064 nm laser (1 W cm^{-2}) for 5 min. The results are shown in Fig. 3a. The temperature increased to 66.3 °C in the case of a solution of Au NPL@TiO_2-4 nanostructures, but only 39.3 °C in the case of an Au NPL@TiO_2-1 solution. Furthermore, the photothermal conversion efficiency of Au NPL@TiO_2-4 nanostructures was calculated by Roper's method. The changes in temperature were recorded as a function of time under continuous irradiation with a 1064 nm

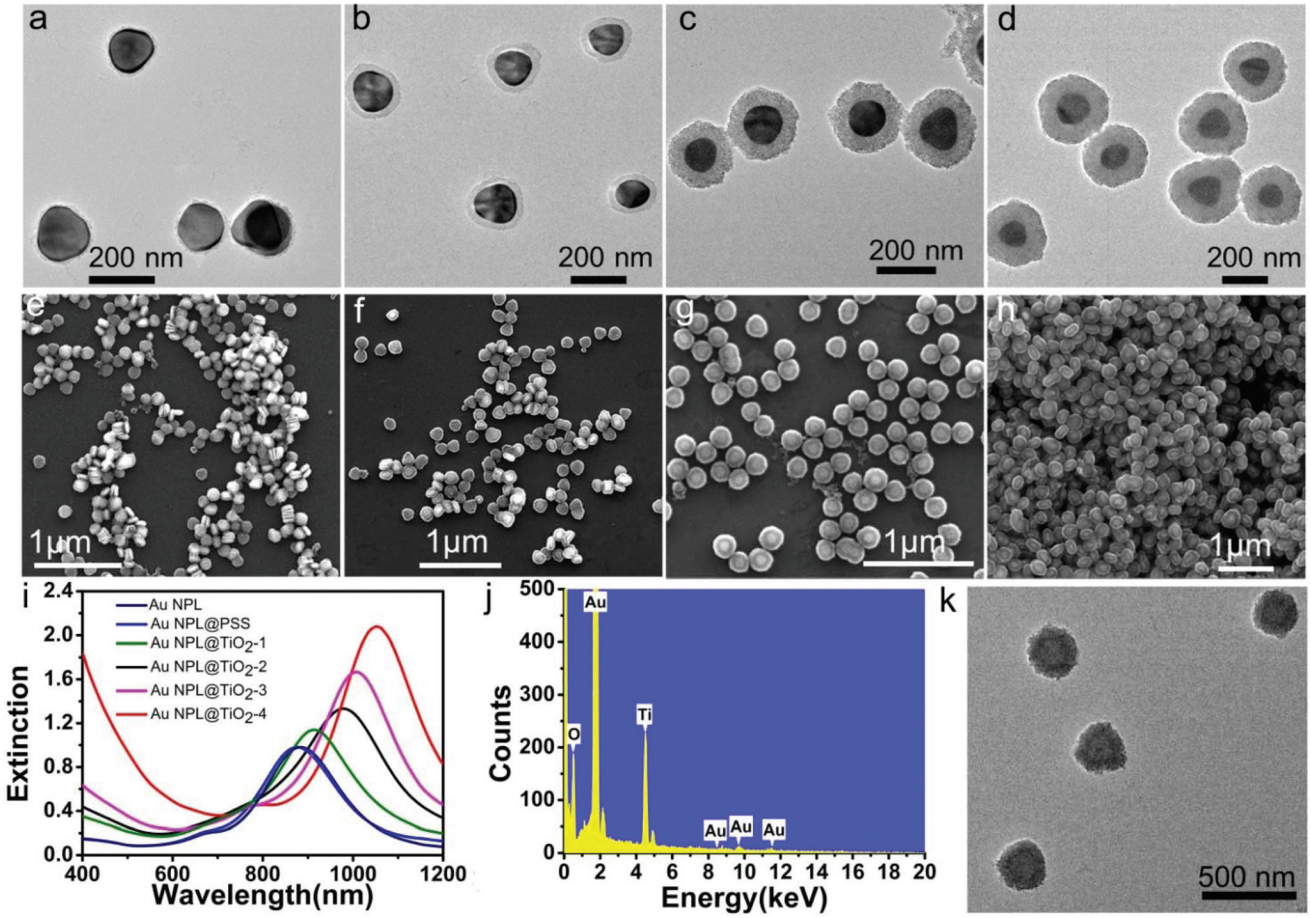

Fig. 2 Au NPL@TiO_2 nanostructures. (a–d) TEM images of Au NPLs coated with TiO_2 shells with different thicknesses (a: Au NPL@TiO_2-1, shell thickness of 10 ± 1 nm, b: Au NPL@TiO_2-2, shell thickness of 28 ± 3 nm, c: Au NPL@TiO_2-3, shell thickness of 49 ± 5 nm, d: Au NPL@TiO_2-4, shell thickness of 68 ± 7 nm). (e–h) Corresponding SEM images of the Au NPL@TiO_2 nanostructures. (i) Extinction spectra of samples of the uncoated Au nanoplates and samples of the corresponding nanostructures coated with shells with different thicknesses. (j) EDS of Au NPL@TiO_2-4 nanostructures. (k) TEM image of TiO_2 shell nanoparticles obtained from Au NPL@TiO_2-4.

laser (1 W cm^{-2}) for 5 min, and the laser was then turned off (Fig. 3b). The heat transfer efficiency was determined during the period in which the temperature decreased and is plotted in Fig. 3c. The Au NPL@TiO_2-4 nanostructures exhibited an excellent photothermal conversion efficiency of 42.05%, which was attributable to the fact that the strong plasmon absorption peak of the Au NPL@TiO_2-4 nanostructures more closely matched the laser wavelength of 1064 nm and thus caused local overheating. The red shift induced by the TiO_2 shell around the Au NPLs was also expected to play a vital role in photothermal conversion in the NIR II region. In addition, even under the same conditions, the Au NPL@TiO_2-4 nanostructures irradiated by a 1064 nm laser exhibited excellent photothermal effect in comparison with when irradiated by an 808 nm laser (Fig. S4†), which demonstrated that the NIR II laser was more appropriate for PTT. Therefore, the Au NPL@TiO_2-4 nanostructures were considered to be suitable candidates for phototherapy *in vitro*.

When excited by external energy, the TiO_2 sonosensitizer subsequently generated electrons and holes, which further reacted with surrounding water and oxygen molecules to generate toxic ROS.[13] In order to boost the effect of sonodynamic therapy using TiO_2, Au NPL@TiO_2 nanostructures were thermally treated at 450 °C to crystallize the amorphous TiO_2 into anatase (Fig. S5†). After thermal treatment, the Au NPL@TiO_2 nanostructures still exhibited a stable morphology with a lattice spacing of 0.35 nm, as determined from an HRTEM image.[37] The ROS-generating capability of Au NPL@TiO_2 nanostructures was investigated by the following method. DPBF, as a probe, was employed to estimate the generation of $^1O_2$ by Au NPL@TiO_2 nanostructures (Fig. 4a). Au NPL@TiO_2-1 nanostructures, Au NPL@TiO_2-2 nanostructures, Au NPL@TiO_2-3 nanostructures, Au NPL@TiO_2-4 nanostructures, TiO_2 shell nanoparticles and Au NPLs were all tested. $^1O_2$ can react with DPBF, which causes a reduction in absorption intensity at a wavelength of 412 nm (Fig. S6†). As shown in Fig. 4a, the Au NPL@TiO_2 nanostructures all exhibited the generation of $^1O_2$, with a decrease in the absorption peak at 412 nm. The absorption intensity of the test solution in the presence of Au NPL@TiO_2-4 nanostructures declined more sharply than in

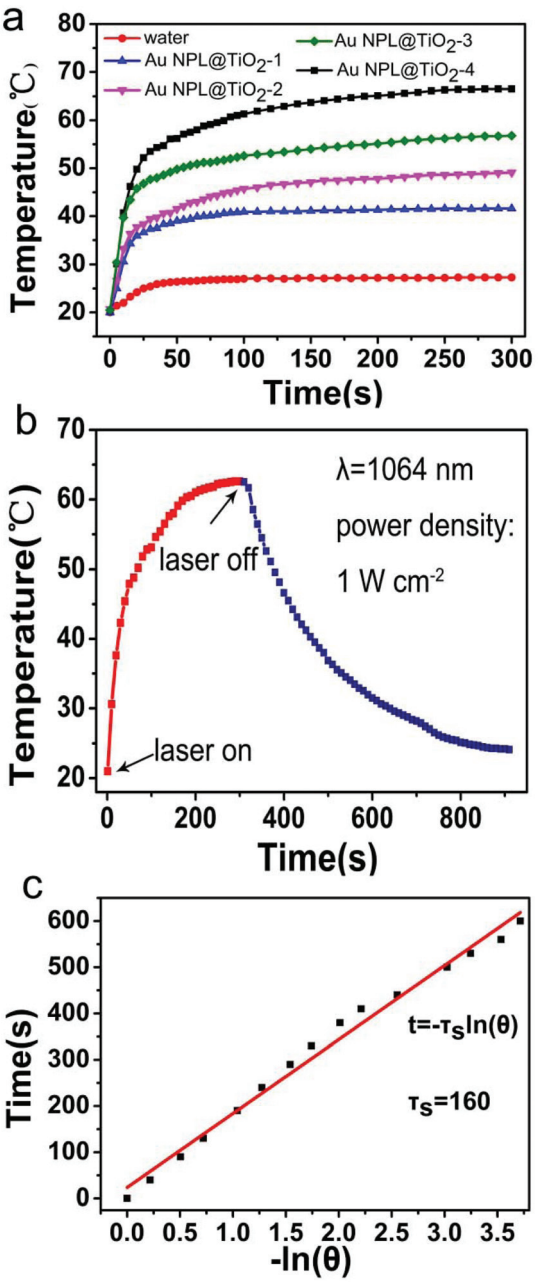

Fig. 3 (a) Changes in the temperature of Au NPL@TiO_2 nanostructures with different shell thicknesses under irradiation by a 1064 nm laser (1 W cm^{-2}) for 5 min (water was used as a blank control). (b) Photothermal effect of an aqueous dispersion of Au NPL@TiO_2-4 (shell thickness: 68 nm) nanostructures irradiated by a 1064 nm laser (1 W cm^{-2}). (c) The time constant for heat transfer from the solution was determined by applying a linearized energy balance to the temperature *versus* the negative natural logarithm of the temperature driving force determined from the cooling stage in (b).

the presence of Au NPL@TiO_2-1 nanostructures, Au NPL@TiO_2-2 nanostructures and Au NPL@TiO_2-3 nanostructures under US irradiation (1.5 W cm^{-2}, 3 MHz, 20 min), which indicated that with an increase in the shell thickness the $^1O_2$ generation capacity increased. To visually observe the

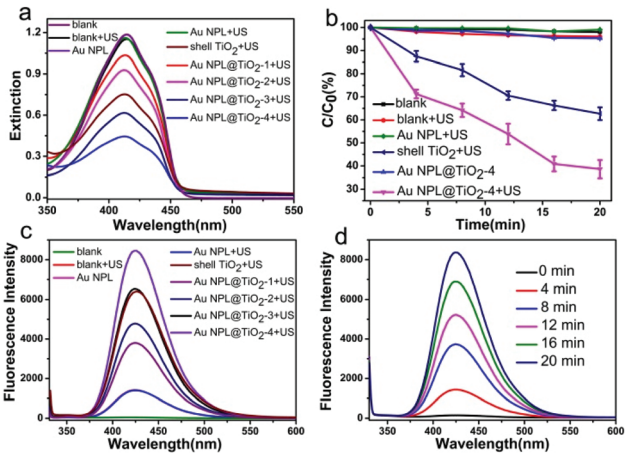

Fig. 4 ROS generation. (a) Absorption spectra of DPBF with sample solutions of Au NPLs, Au NPL@TiO_2 nanostructures and TiO_2 shell nanoparticles under US activation. (b) Normalized reductions in the absorbance of DPBF at 412 nm as functions of time. (c) Fluorescence spectra of solutions of Au NPLs, Au NPL@TiO_2 nanostructures and TiO_2 shell nanoparticles in the presence of TA under US activation. (d) Changes in the fluorescence intensity of TA in the presence of Au NPL@TiO_2-4 (shell thickness: 68 nm) nanostructures at an excitation wavelength of 315 nm under US activation for up to 20 min.

$^1O_2$ generation behaviour, the decay rate of the strongest absorption peak at 412 nm as a function of time is plotted in Fig. 4b. After US irradiation for 20 min, only a slight decrease was observed in the Au NPLs and blank groups. However, the Au NPL@TiO_2-4 nanostructures group displayed a rapid decrease, and the intensity declined to 71% over the first 5 min and eventually reached 38% at 20 min under US irradiation, which was, significantly, about twice that in the case of TiO_2 shell nanoparticles under US irradiation. It is noteworthy that there was an enhancement in $^1O_2$ generation ability in the case of Au NPL@TiO_2-4 nanostructures in comparison with TiO_2 shell nanoparticles.

TA, as a fluorescent probe, was used to detect the generation of $^{\bullet}OH$ by Au NPL@TiO_2 nanostructures (Fig. S7†). As shown in Fig. 4c, very weak fluorescence was detected from Au NPLs and TiO_2 shell nanoparticles after US irradiation for 20 min. In contrast, a fluorescence emission that was more than 5 times stronger was measured in the case of Au NPL@TiO_2-4 nanostructures, and the generation of $^{\bullet}OH$ gradually increased over time, as shown in Fig. 4d, which illustrated the effective production of $^{\bullet}OH$ by Au NPL@TiO_2-4 nanostructures under US irradiation. The foregoing results clearly show that the Au NPL@TiO_2 nanostructures exhibited effective enhancement of the generation of both $^1O_2$ and $^{\bullet}OH$ under US excitation in comparison with TiO_2 shell nanoparticles.

An illustration of the mechanism of the enhancement in SDT is shown in Fig. S8.† When TiO_2 was activated by ultrasound, it underwent charge separation and the valence band electrons (e^-) were excited into the conduction band of TiO_2, which left positively charged holes (h^+). Because the Fermi level of Au is lower than that of TiO_2, Au served as an acceptor

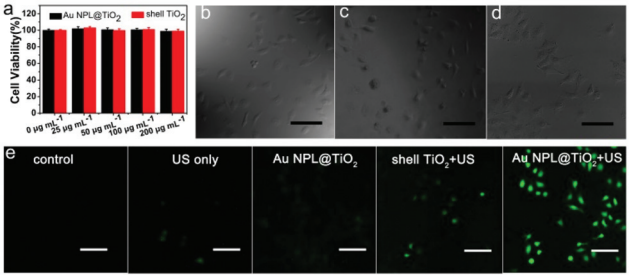

Fig. 5 Biocompatibility effect. (a) Cell viability observed when TiO_2 shell nanoparticles obtained from Au NPL@TiO_2 and Au NPL@TiO_2 nanostructures with a shell thickness of 68 nm at different concentrations were co-incubated with HeLa cells for 24 h. (b) Microscopy images of HeLa cells, scale bar: 50 μm. (c, d) Microscopy images of HeLa cells after incubation with TiO_2 shell nanoparticles and Au NPL@TiO_2 nanostructures (shell thickness of 68 nm) for 24 h. Scale bar: 50 μm. (d) Fluorescence images of HeLa cells stained with DCFH-DA after different treatments (the control group was treated with PBS). Scale bar: 50 μm.

of the e^- transferred from the TiO_2 shell, while the h^+ remained in TiO_2.[38,39] As a consequence, Au extensively suppressed the recombination of e^-/h^+ pairs, and the lifetime of electrons became prolonged. The e^- on the surface of TiO_2 were trapped *via* O_2 to form superoxide ($O_2^{\bullet-}$), which reacted with holes in the valence band to give $^1O_2$, while H_2O reacted with holes to form hydroxyl radicals ($^{\bullet}OH$).[12,40,41] In this way, the strong interaction between Au and TiO_2 resulted in a remarkable enhancement in the yield of ROS.

To determine the cytotoxicity of Au NPL@TiO_2 nanostructures (shell thickness: 68 nm), a standard CCK-8 cell viability assay was conducted. Without laser treatment, different concentrations of Au NPL@TiO_2 nanostructures (0, 25, 50, 100, and 200 μg mL^{-1}) were incubated with HeLa cells for 24 h. After endocytosis by cancer cells, the cell viabilities all exceeded 95% and no significant cytotoxicity was observed, according to the CCK-8 assay (Fig. 5a). Optical images of HeLa cells before and after incubation with TiO_2 shell nanoparticles

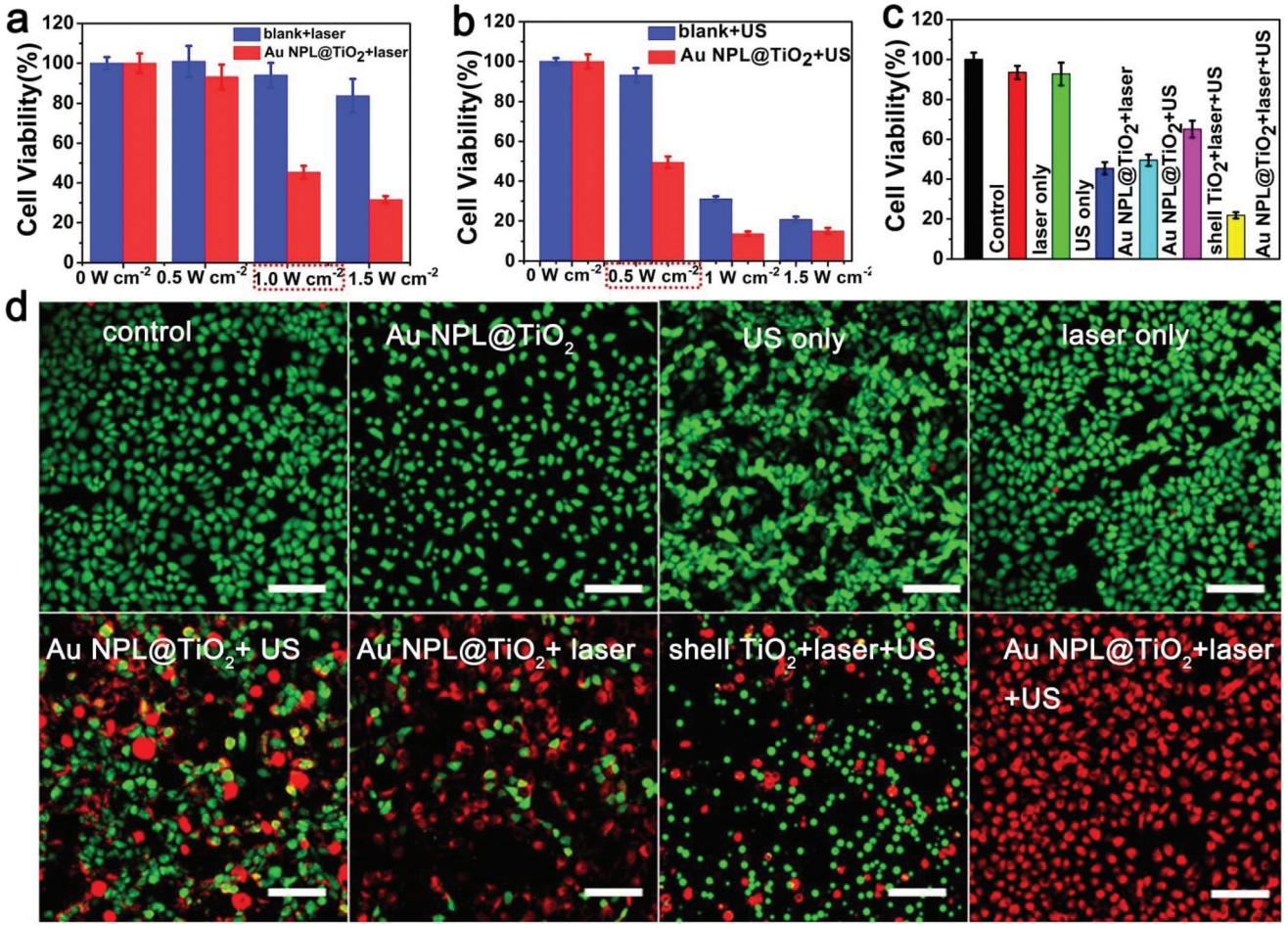

Fig. 6 Synergetic therapeutic effect. (a, b) Viability of HeLa cells co-incubated with Au NPL@TiO_2 nanostructures (shell thickness: 68 nm) at different 1064 nm laser power densities (0, 0.5, 1.0, and 1.5 W cm^{-2}) and different US power densities (0, 0.5, 1.0, and 1.5 W cm^{-2}). The red dashed lines in a and b indicate the appropriate laser power density and US power density. (c) Viability of HeLa cells incubated with Au NPL@TiO_2 nanostructures and TiO_2 shell nanoparticles after different treatments. (d) Confocal fluorescence microscopy images of HeLa cells (incubated with Au NPL@TiO_2 nanostructures and TiO_2 shell nanoparticles) stained with calcein AM and PI after different treatments (green: live cells, red: dead cells), scale bar: 100 μm.

and Au NPL@TiO_2 nanostructures (100 μg mL^{-1}) are shown in Fig. 5b and c, respectively. After 24 h, the morphology of HeLa cells remained robust, which demonstrated the excellent biocompatibility and low cytotoxicity of the Au NPL@TiO_2 nanostructures in HeLa cells. Furthermore, after thermal treatment at 450 °C, CTAB in the Au NPL@TiO_2 nanostructures was totally removed, as CTAB decomposed at 300 °C (Fig. S9†), which laid a foundation for *in vitro* and *in vivo* applications.

To ensure the intracellular SDT performance of Au NPL@TiO_2 nanostructures (100 μg mL^{-1}) under US activation, DCFH-DA was used to detect the generation of ROS by monitoring green fluorescence in HeLa cells, in which DCFH was oxidized to green fluorescent DCF in the presence of ROS. Not surprisingly, the control group (without any treatment) exhibited negligible fluorescence, whereas remarkable green fluorescence was observed in the Au NPL@TiO_2 + US group, which was much brighter than that in the TiO_2 shell nanoparticles + US group and

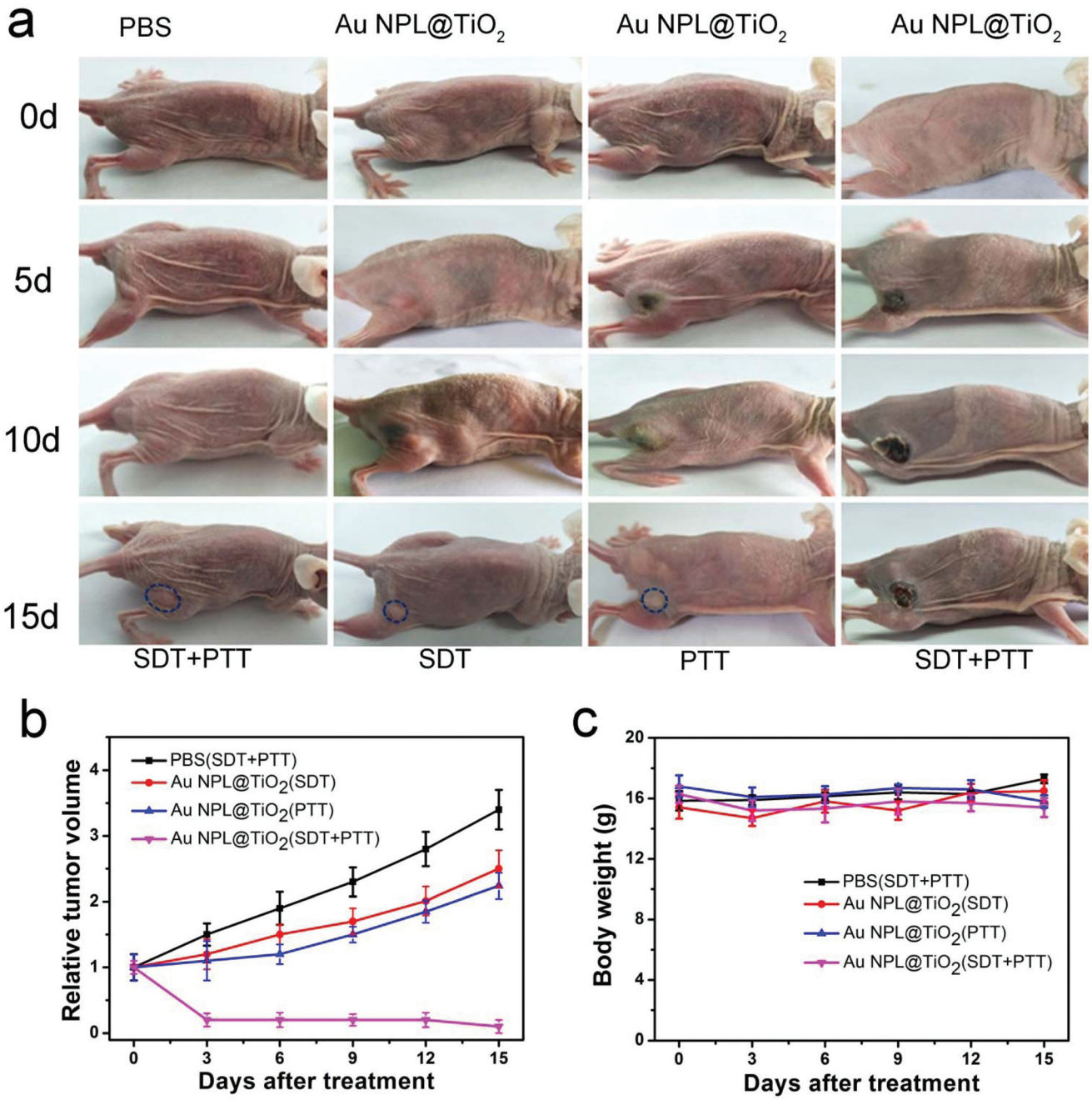

Fig. 7 (a) Representative pictures of mice treated with various samples and irradiated with a 1064 nm laser: 1 W cm^{-2}, 5 min or by SDT: 0.5 W cm^{-2}, 4 min on/1 min off, repeated 5 times. The blue dashed lines indicate the tumours in the mice. Curves of (b) relative tumour growth and (c) body weight after various treatments.

the Au NPL@TiO_2 nanostructures group (Fig. 5d), which indicated the potential for SDT in anticancer therapy.

On the basis of the remarkable photothermal and sonodynamic properties of the Au NPL@TiO_2 nanostructures, their therapeutic effect in cancer cells was assessed by a CCK-8 assay under US and laser activation. As shown in Fig. 6a, after exposure to a 1064 nm laser (5 min) for PTT, the viability of HeLa cells was shown to be dependent on the laser power density, and the cells were predominantly killed after co-incubation with Au NPL@TiO_2 nanostructures (100 μg mL^{-1}) as PTT agents. The viability of cancer cells co-incubated with Au NPL@TiO_2 nanostructures reached 31.8% at 1.5 W cm^{-2} in comparison with 93.2% at 0.5 W cm^{-2}. However, in comparison with the viability of 83.7% observed in the case of blank control cells under exposure to a laser at 1.5 W cm^{-2}, blank cells exhibited a viability of 95.4% with negligible cytotoxicity under exposure to a laser at 1.0 W cm^{-2}. Therefore, 1.0 W cm^{-2} was regarded as the appropriate power density for PTT, with a considerable death rate and a low power density.

On the other hand, different US power densities were also employed. Under US excitation at a power density of 1.5 W cm^{-2}, significant cytotoxicity was observed in the Au NPL@TiO_2 nanostructures and blank groups (Fig. 6b). The viability of cells treated with Au NPL@TiO_2 nanostructures was 14.7% and the viability of blank cells was 20.9% after treatment at 1.5 W cm^{-2} for 20 min, which largely resulted from the heat produced during the US irradiation. A relatively high cell viability of 93.1% in the case of blank cells and effective SDT with a cell viability of 48.5% after treatment with Au NPL@TiO_2 nanostructures were observed at a US power density of 0.5 W cm^{-2}. As a result, a US power density of 0.5 W cm^{-2} was optimal for further study because it led to low cytotoxicity in blank cells and killed cells treated with Au NPL@TiO_2 nanostructures.

Owing to the significant photothermal and sonodynamic properties of the Au NPL@TiO_2 nanostructures under single-energy activation, it was sensible to combine PTT (1064 nm, 1 W cm^{-2}, 5 min) with SDT (0.5 W cm^{-2}, 3 MHz, 20 min) to increase their therapeutic efficiency with low and safe power dosages. Fig. 6c shows that the cell viability was only 20.3% after treatment with Au NPL@TiO_2 nanostructures with PTT and SDT, in comparison with a cell viability of 45.3% after PTT alone and a cell viability of 50.2% after SDT alone, which demonstrated that synergistic therapy was fatal to cancer cells. In addition, in comparison with the cell viability of 65.1% observed after treatment with TiO_2 shells with PTT and SDT, the Au NPL@TiO_2 nanostructures were more appropriate for synergetic therapy. From staining live and dead cells after treatment, almost all cells were dead after being treated with Au NPL@TiO_2 + laser + US, as seen in Fig. 6d, whereas some live cells were observed after being treated with Au NPL@TiO_2 + SDT, Au NPL@TiO_2 + PTT or TiO_2 shells + laser + US, as shown by the green dots. This clearly showed the superiority of the combination therapy over the single treatments, which implied that the Au NPL@TiO_2 nanostructures were effective therapeutic agents against cancer cells.

Finally, the *in vivo* therapeutic effect of the Au NPL@TiO_2 nanostructures was assessed. Four groups of HeLa tumor-bearing nude mice were used in the experiment (Fig. 7). The mice intravenously injected with PBS under dual irradiation (SDT: 0.5 W cm^{-2}, 4 min on/1 min off, repeated 5 times; PTT: 1064 nm laser, 1 W cm^{-2}, 5 min) at the tumour site were the control group. The mice in the experimental groups were treated with single irradiation (PTT: 1064 nm laser, 1 W cm^{-2}, 5 min or SDT: 0.5 W cm^{-2}, 4 min on/1 min off, repeated 5 times) and dual irradiation (SDT: 0.5 W cm^{-2}, 4 min on/1 min off, repeated 5 times; PTT: 1064 nm laser, 1 W cm^{-2}, 5 min) at the tumour site. The mean tumour growth volume in each group was monitored during the evaluation period of 15 days. As shown in Fig. 7a and b, the mice in the PBS group exhibited obvious tumour growth after being treated with SDT and PTT for 15 days. In comparison with the control group, after 15 days the mice treated with SDT and PTT exhibited the most effective suppression of tumour growth and the tumor was nearly eliminated, even with a burning scar. The single SDT and PDT treatment groups also exhibited some therapeutic effects in comparison with the PBS group, although these effects were inferior to those of the SDT + PTT combination. In addition, no obvious changes in the body weights of the mice were observed over the period of 15 days (Fig. 7c), which indicated the safety of the Au NPL@TiO_2 nanostructures.

Conclusions

In summary, synergetic anticancer therapeutic agents that combined PTT with enhanced SDT were successfully prepared on the basis of the strong plasmon absorption of Au NPL@TiO_2 nanostructures in the NIR II region. In the presence of TiO_2 shells with different thicknesses, Au NPLs exhibited red shifts to the NIR II region and achieved a photothermal conversion efficiency of 42.05%. Moreover, the yield of ROS from TiO_2 was greatly improved by the electron traps in the Au NPLs. The synergistic photothermal and sonodynamic effects of the Au NPL@TiO_2 nanostructures were further studied for anticancer therapy *in vitro* and *in vivo*. A CCK-8 assay and microscopy images demonstrated the non-toxicity and high biocompatibility of the Au NPL@TiO_2 nanostructures in HeLa cells. Significantly, synergetic photothermal and sonodynamic therapy led to a cell viability of only 20.3% after treatment with Au NPL@TiO_2 nanostructures *in vitro*. Tumours were also totally eliminated *in vivo* experiments. We believe that our proposed Au NPL@TiO_2 core–shell nanostructures, which play dual roles as photothermal/sonodynamic nanoagents, will be highly promising in anticancer therapy and may open up a new avenue in the clinical treatment of tumours in the NIR-II biological window.

Statement

All animal procedures were performed in accordance with the National Institutes of Health Animal Care and Use Guidelines

and were approved by the Animal Ethics Committee of Huanghe Science and Technology College.

Conflicts of interest

There are no conflicts to declare.

Acknowledgements

The authors thank Minhui Wen and Min Wu from the Institute of Nanostructured Functional Materials, Huanghe Science and Technology College for the assistance with cell experiments. The authors also thank Guizhou Medical University for the help of mice experiments. This research was supported by the National Natural Science Foundation of China (51702114), Natural Science Foundation of Henan Province (172102210381) and Natural Science Foundation of the Education Department of Henan Province (18A150011).

Notes and references

1 E. B. Dickerson, E. C. Dreaden, X. Huang, I. H. El-Sayed, H. Chu, S. Pushpanketh, J. F. McDonald and M. A. El-Sayed, *Cancer Lett.*, 2008, **269**, 57–66.
2 P. Vijayaraghavan, C. H. Liu, R. Vankayala, C. S. Chiang and K. C. Hwang, *Adv. Mater.*, 2014, **26**, 6689–6695.
3 A. M. Smith, M. C. Mancini and S. Nie, *Nat. Nanotechnol.*, 2009, **4**, 710–711.
4 W. Shao, G. Chen, A. Kuzmin, H. L. Kutscher, A. Pliss, T. Y. Ohulchanskyy and P. N. Prasad, *J. Am. Chem. Soc.*, 2016, **138**, 16192–16195.
5 G. Chen, J. Shen, T. Y. Ohulchanskyy, N. J. Patel, A. Kutikov, Z. Li, J. Song, R. K. Pandey, H. Agren and P. N. Prasad, *ACS Nano*, 2012, **6**, 8280–8287.
6 Y. Jiang, J. Li, X. Zhen, C. Xie and K. Pu, *Adv. Mater.*, 2018, **30**, 1705980–1705986.
7 X. Han, J. Huang, X. Jing, D. Yang, H. Lin, Z. Wang, P. Li and Y. Chen, *ACS Nano*, 2018, **12**, 4545–4555.
8 A. N. Bashkatov, E. A. Genina, V. I. Kochubey and V. V. Tuchin, *J. Phys. D: Appl. Phys.*, 2005, **38**, 2543–2555.
9 G. Hong, Y. Zou, A. L. Antaris, S. Diao, D. Wu, K. Cheng, X. Zhang, C. Chen, B. Liu, Y. He, J. Z. Wu, J. Yuan, B. Zhang, Z. Tao, C. Fukunaga and H. Dai, *Nat. Commun.*, 2014, **5**, 4206–4214.
10 Y. Jiang, P. K. Upputuri, C. Xie, Y. Lyu, L. Zhang, Q. Xiong, M. Pramanik and K. Pu, *Nano Lett.*, 2017, **17**, 4964–4969.
11 T. Yang, Y. Tang, L. Liu, X. Lv, Q. Wang, H. Ke, Y. Deng, H. Yang, X. Yang, G. Liu, Y. Zhao and H. Chen, *ACS Nano*, 2017, **11**, 1848–1857.
12 V. G. Deepagan, D. G. You, W. Um, H. Ko, S. Kwon, K. Y. Choi, G. R. Yi, J. Y. Lee, D. S. Lee, K. Kim, I. C. Kwon and J. H. Park, *Nano Lett.*, 2016, **16**, 6257–6264.
13 C. Dai, S. Zhang, Z. Liu, R. Wu and Y. Chen, *ACS Nano*, 2017, **11**, 9467–9480.
14 X. Qian, Y. Zheng and Y. Chen, *Adv. Mater.*, 2016, **28**, 8097–8129.
15 I. Rosenthal, J. Z. Sostaric and P. Riesz, *Ultrason. Sonochem.*, 2004, **11**, 349–363.
16 K. Cheng, M. Sano, C. H. Jenkins, G. Zhang, D. Vernekohl, W. Zhao, C. Wei, Y. Zhang, Z. Zhang, Y. Liu, Z. Cheng and L. Xing, *ACS Nano*, 2018, **12**, 4946–4958.
17 Y.-W. Chen, T.-Y. Liu, P.-H. Chang, P.-H. Hsu, H.-L. Liu, H.-C. Lin and S.-Y. Chen, *Nanoscale*, 2016, **8**, 12648–12657.
18 M. El-Fray, A. Piegat and P. Prowans, *Adv. Eng. Mater.*, 2009, **11**, B200–B203.
19 L. Ma, Y. Huang, M. Hou, Z. Xie and Z. Zhang, *Sci. Rep.*, 2015, **5**, 15442–15449.
20 C. Fang, H. Jia, S. Chang, Q. Ruan, P. Wang, T. Chen and J. Wang, *Energy Environ. Sci.*, 2014, **7**, 3431–3438.
21 X. Kang, Q. Ruan, H. Zhang, F. Bao, J. Guo, M. Tang, S. Cheng and J. Wang, *Nanoscale*, 2017, **9**, 5879–5886.
22 H. Jia, X. M. Zhu, R. Jiang and J. Wang, *ACS Appl. Mater. Interfaces*, 2017, **9**, 2560–2571.
23 H. Y. Wan, J. L. Chen, X. Zhu, L. Liu, J. Wang and X. M. Zhu, *Adv. Sci.*, 2018, **5**, 1700585–1700598.
24 F. Gao, M. Sun, L. Xu, L. Liu, H. Kuang and C. Xu, *Adv. Funct. Mater.*, 2017, **27**, 1700605–1700610.
25 C. Li, Y. Zhang, Z. Li, E. Mei, J. Lin, F. Li, C. Chen, X. Qing, L. Hou, L. Xiong, H. Hao, Y. Yang and P. Huang, *Adv. Mater.*, 2018, **30**, 1706150–1706157.
26 A. Kumar, S. Kumar, W. K. Rhim, G. H. Kim and J. M. Nam, *J. Am. Chem. Soc.*, 2014, **136**, 16317–16325.
27 Y. Liu, Z. Wang, Y. Liu, G. Zhu, O. Jacobson, X. Fu, R. Bai, X. Lin, N. Lu, X. Yang, W. Fan, J. Song, Z. Wang, G. Yu, F. Zhang, H. Kalish, G. Niu, Z. Nie and X. Chen, *ACS Nano*, 2017, **11**, 10539–10548.
28 S. Huang, S. Duan, J. Wang, S. Bao, X. Qiu, C. Li, Y. Liu, L. Yan, Z. Zhang and Y. Hu, *Adv. Funct. Mater.*, 2016, **26**, 2532–2544.
29 F. Qin, T. Zhao, R. Jiang, N. Jiang, Q. Ruan, J. Wang, L.-D. Sun, C.-H. Yan and H.-Q. Lin, *Adv. Opt. Mater.*, 2016, **4**, 76–85.
30 W. H. Lin, Y. H. Lu and Y. J. Hsu, *J. Colloid Interface Sci.*, 2014, **418**, 87–94.
31 Y. Ni, C. Kan, J. Xu and Y. Liu, *Superlattices Microstruct.*, 2018, **114**, 124–142.
32 X. Cui, F. Qin, Q. Ruan, X. Zhuo and J. Wang, *Adv. Funct. Mater.*, 2018, **28**, 1705516–1705528.
33 N. M. Andoy, X. Zhou, E. Choudhary, H. Shen, G. Liu and P. Chen, *J. Am. Chem. Soc.*, 2013, **135**, 1845–1852.
34 S. Chen, P. Xu, Y. Li, J. Xue, S. Han, W. Ou, L. Li and W. Ni, *Nano-Micro Lett.*, 2016, **8**, 328–335.
35 S. R. Beeram and F. P. Zamborini, *ACS Nano*, 2010, **4**, 3633–3646.
36 J. Han, J. Zhang, M. Yang, D. Cui and J. M. de la Fuente, *Nanoscale*, 2016, **8**, 492–499.
37 W. Wu, X. Xue, X. Jiang, Y. Zhang, Y. Wu and C. Pan, *AIP Adv.*, 2015, **5**, 057105–057112.

38 O. Ola and M. M. Maroto-Valer, *J. Photochem. Photobiol., C*, 2015, **24**, 16–42.
39 M. Abdulla-Al-Mamun, Y. Kusumoto, T. Zannat and M. S. Islam, *Phys. Chem. Chem. Phys.*, 2011, **13**, 21026–21034.
40 Y. Nosaka, T. Daimon, A. Y. Nosaka and Y. Murakami, *Phys. Chem. Chem. Phys.*, 2004, **6**, 2917–2918.
41 G. Canavese, A. Ancona, L. Racca, M. Canta, B. Dumontel, F. Barbaresco, T. Limongi and V. Cauda, *Chem. Eng. J.*, 2018, **340**, 155–172.